

# Structural, electrical and optical properties of transparent conductive titanium–gallium–zinc oxide films by magnetron sputtering

Zhou Lu<sup>1,2</sup> · H. Kang<sup>1,2</sup> · Z. Zhong<sup>1,2</sup> · T. Zhang<sup>1,2</sup>

Received: 9 May 2016 / Accepted: 1 August 2016 / Published online: 24 August 2016  
© Springer Science+Business Media New York 2016

**Abstract** The transparent semiconductors of titanium–gallium–zinc oxide (TiGa–ZnO) thin films were prepared on glass substrates by radio frequency (rf) magnetron sputtering. The dependence of the grain-growth orientation, structure, electrical and optical properties of thin films on rf power was investigated by X-ray diffractometer, UV–visible spectrophotometer and Hall effect measurement system. Experimental results show that all nanocrystalline TiGa–ZnO thin films possess preferential orientation along the (002) plane. The rf power strongly affects the crystal structure, electrical and optical properties of thin films. When the rf power is at 190 W, the thin film deposited on the glass substrates has the optimal crystal quality and optoelectronic properties, with the largest mean grain size (83.1 nm), the minimum lattice strain ( $6.287 \times 10^{-4}$ ), the highest average transmittance in the visible range (84.62 %), the lowest electrical resistivity ( $9.68 \times 10^{-4} \Omega \text{ cm}$ ) and the maximum figure of merit ( $6.173 \times 10^3 \Omega^{-1} \text{ cm}^{-1}$ ). The optical bandgaps of thin films were evaluated by extrapolation method and observed to increase firstly and then decrease with the increment of rf power. Furthermore, the optical parameters including refractive index, extinction coefficient, dielectric constant

and dissipation factor of the thin films were determined by the pointwise unconstrained optimization method. The dispersion behaviour of refractive index was also analyzed using the Wemple–DiDomenico single-oscillator theory.

## 1 Introduction

Zinc oxide (ZnO) is a II–VI group semiconductor material with wide direct bandgap and wurtzite structure. The high stability, melting point and excitation energy make it a promising ultraviolet and blue optoelectronic material. In addition, the ZnO-based semiconductor thin films offer a wide range of applications in a variety of optoelectronic devices such as solar cells [1–3], light-emitting diodes (LEDs) [4–6], thin films transistors (TFTs) [7, 8], flat panel displays (FPDs) [9, 10], touch screens [11], gas sensors [12–14] and resistive switching [15]. A transparent conductive electrode is a necessary component of LEDs and solar cells. Usually, it consists of a transparent conducting oxide (TCO) thin film and a glass substrate. The most important commercial material for TCOs nowadays is tin-doped indium oxide (ITO), owing to its outstanding characteristics of high optical transmittance, low electrical resistivity, high infrared reflectance and absorbance in the microwave region. However, ITO is likely to become unavailable because the fast-growing semiconductor industries are faced with the scarcity of indium (In) resources and toxicity in the atmosphere. In view of the depletion of ITO, the ZnO-based TCOs will be emerging as an alternative transparent electrode. Recently, much attention has been paid to the codoping process in which the two elements are doped into ZnO simultaneously, because the codoped ZnO thin films are expected to show some improvements in optical and electrical performance

✉ Zhou Lu  
zetalambda@163.com

✉ Z. Zhong  
longscun@126.com

<sup>1</sup> College of Electronic Information Engineering,  
South-Central University for Nationalities, Wuhan 430073,  
People's Republic of China

<sup>2</sup> Hubei Key Laboratory of Intelligent Wireless  
Communications, South-Central University for Nationalities,  
Wuhan 430073, People's Republic of China

of TCOs. Suzuki et al. [16] proposed that codoping method had the advantage to improve the properties of aluminum-doped ZnO thin film. They prepared the vanadium–aluminum codoped ZnO thin films by direct current (dc) magnetron sputtering to enhance the corrosion-resistance of the TCO thin films. Kirby and Van Dover [17] deposited the indium–aluminum codoped ZnO thin films using off-axis reactive radio frequency (rf) sputtering and obtained improved electrical properties with no degradation in optical transmittance. Suresh et al. [18] prepared the indium–gallium codoped ZnO thin films by pulsed laser deposition and achieved improved surface morphology with enhanced optoelectrical properties. Up to now, the aluminum–titanium [19], magnesium–aluminum [20], boron–gallium [21], lithium–magnesium [22], aluminum–gallium [23] and magnesium–gallium [24] codoping cases have also been reported. However, there have been few reports on titanium–gallium codoped ZnO (TiGa–ZnO) thin films.

For the preparation of doped ZnO thin films, there are many deposition techniques currently in use, for example, rf magnetron sputtering [25–28], dc magnetron sputtering [29, 30], hydrothermal process [31], molecular beam epitaxy [32], reactive plasma deposition [33] and pulsed laser ablation [34]. Among the deposition techniques, conventional rf magnetron sputtering has some advantages in comparison with the other methods. This technique is quite simple and the required setup is less expensive, and it is considered to be the most available deposition method to obtain highly uniform films with high packing density and strong adhesion at a high deposition rate [35].

In this present work, transparent conducting TiGa–ZnO thin films were deposited on glass substrates by rf magnetron sputtering technique. The effects of rf power on the grain-growth orientation, microstructure, electrical and optical properties of the thin films were investigated by X-ray diffractometer, UV–visible spectrophotometer and Hall effect measurement system.

## 2 Experimental procedure

The commercial plane glass (CSG Holding Co. Ltd) was cut into 50 mm × 50 mm plates and used as substrates in this experiment. Prior to their use, the glass substrates were successively washed in an ultrasonic bath of acetone, alcohol and deionized water, each for 15 min, and then dried in a high-purity (99.999 % in purity) nitrogen gas jet.

The TiGa–ZnO thin films were deposited on the cleaned glass substrates by using 13.56 MHz rf magnetron sputtering (MS-560C). A sintered ceramic target (1 wt% TiO<sub>2</sub>: 2 wt% Ga<sub>2</sub>O<sub>3</sub>: 97 wt% ZnO, 4 N purity) was employed as source material. The sputtering chamber was evacuated to

a base pressure below  $5.4 \times 10^{-4}$  Pa before argon gas. After vacuum pumping, the sputtering argon gas with a purity of 99.999 % was introduced into the chamber and controlled by the standard mass flow controllers (MFCs). The MFCs have accuracy of 1 % of the maximum value (50 sccm). Before the TiGa–ZnO thin films deposition, pre-sputtering was conducted for about 12 min to attain stability and to remove impurities. The deposition parameters for preparing TiGa–ZnO thin films were as follows: the target-substrate distance, 70 mm; the substrate temperature, 570 K; the argon gas flow rate, 30 sccm; and the argon gas pressure, 0.5 Pa. In order to study the influence of rf power on the structure and properties of thin films, the rf power ( $P_{\text{rf}}$ ) was varied from 140 to 215 W.

The crystallographic and phase structure of the deposited samples were characterized by X-ray diffraction (XRD). A D8-Advance diffractometer with Cu K $\alpha$  source ( $\lambda = 0.15406$  nm) and Ni filter was used for the XRD measurements. The power of XRD was 1200 W and the scan was performed from 20° to 80° at a speed of 1.872° min<sup>-1</sup>, with a step size of 0.0164°. The crystallite phase was determined with the data of joint committee on powder diffraction standards (JCPDS). The thickness was measured by a surface profiler (Alpha-step 500). The electrical properties of the samples were characterized by a Hall effect measurement system (RH-2035) using the Van der Pauw configuration. The optical transmission spectra were recorded with a double-beam UV–visible spectrophotometer (TU-1901), and the optical constants of samples were determined from the transmission spectra using the pointwise unconstrained optimization method [36, 37]. All measurements were carried out in ambient air at room temperature.

## 3 Results and discussion

Figure 1 shows the XRD patterns ( $\theta$ – $2\theta$ ) of the TiGa–ZnO samples deposited on glass substrates at different rf powers  $P_{\text{rf}}$ . These XRD peaks are assigned to ZnO according to the JCPDS data File No. 36-1451 (ZnO). All the samples exhibit a dominant (002) peak with slight (100) and (004) peaks in the displayed  $2\theta$  region, indicating that the obtained thin films have a preferred orientation with the  $c$ -axis perpendicular to the substrate surface, regardless of the rf power. No extra phases related with titanium, gallium and zinc compound were detected from the XRD patterns, which implies that the dopants have not destroyed the ZnO structure and act as typical dopants. From Fig. 1, the intensity of (002) peak is much stronger than the others. Corresponding to the rf power of 140, 165, 190 and 215 W, the intensity of (002) peak ( $I_{(002)}$ ) are observed to be about  $6.19 \times 10^5$ ,  $1.40 \times 10^6$ ,  $1.92 \times 10^6$  and  $1.19 \times 10^6$  cps

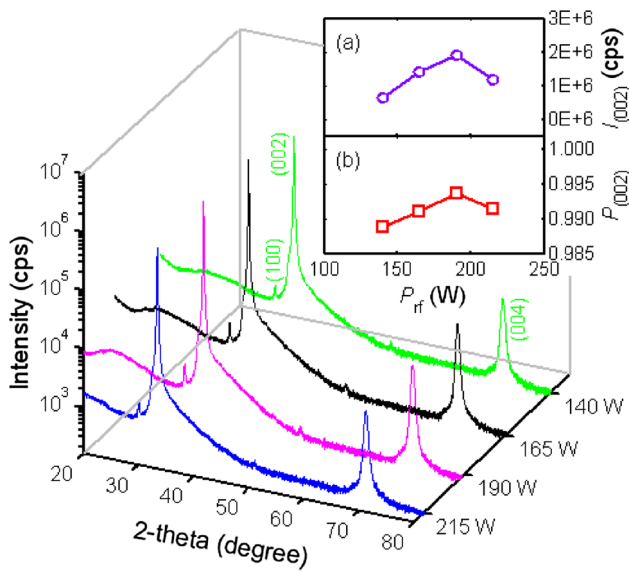


**Fig. 1** XRD patterns of the thin films deposited at different rf powers. The insets show the variation of  $I_{(002)}$  and  $P_{(002)}$  as a function of rf power for the thin films

respectively, as shown in the inset of Fig. 1. Clearly, the intensity of (002) peak rises initially and then falls with the increase of rf power. The TiGa–ZnO thin film prepared at the rf power of 190 W has the maximum intensity of (002) peak. According to the literature, the relative intensity of (002) peak can characterize the degree of texture of ZnO-based thin film with its *c*-axis perpendicular to substrate which will enhance the charge transport [38]. The degree of preferred (002) orientation of the thin films can be defined with the orientation factor  $P_{(002)}$  [39]:

$$P_{(002)} = \frac{I_{(002)}}{\sum I_{(hkl)}}, \tag{1}$$

where the subscript *h*, *k* and *l* are Miller indices,  $I_{(002)}$  is the intensity of (002) peak, and  $\sum I_{(hkl)}$  is the sum of the intensities of all the diffraction peaks. The value of  $P_{(002)}$  is unity for a perfectly (002) oriented thin film [40]. The variation of orientation factor  $P_{(002)}$  with rf power for the deposited thin films is presented in the inset of Fig. 1. As can be seen, all the deposited thin films exhibit (002) as the preferred orientation. This (002) preferred orientation is due to the fact that the most densely packed (002) plane in wurtzite ZnO has the lowest surface free energy [41]. With increasing the rf power from 145 to 190 W, the  $P_{(002)}$  increases continuously, indicating that the crystal quality of the TiGa–ZnO thin films appears to become better. However, with further increase from 190 to 215 W, the  $P_{(002)}$  decreases slightly and the crystal quality deteriorates. The maximal  $P_{(002)}$  of 0.9937 is obtained when the rf power is 190 W. The results indicate that the TiGa–ZnO thin films deposited at the rf power of 190 W possesses the best crystallite quality.

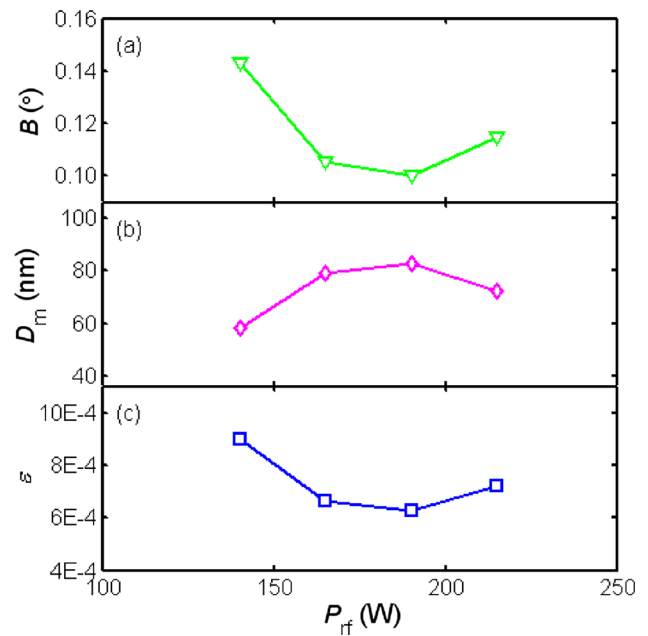


**Fig. 2** The values of  $B$ ,  $D_m$  and  $\epsilon$  for the thin films deposited at different rf powers

Figure 2a presents the full-width at half-maximum (FWHM,  $B$ ) of (002) peak for the TiGa–ZnO samples deposited on glass substrates at different rf powers  $P_{rf}$ . Note that the  $B$  decreases significantly with rf power up to 190 W, and then it increases slightly above 190 W. The decrease of the  $B$  indicates the increase of grain size of the deposited thin films. The mean grain size ( $D_m$ ) can be estimated according to the Debye–Scherrer formula [42]:

$$D_m = \frac{K\lambda}{(\pi B/180) \cos(\pi\theta/180)}, \tag{2}$$

where  $K$  is the shape factor equal to 0.90,  $\lambda$  is the wavelength of incident X-rays,  $B$  is the FWHM measured in degrees and  $\theta$  is the Bragg’s diffraction angle at peak position in degrees. The lattice strain ( $\epsilon$ ) was evaluated using the following equation [43, 44]:

$$\epsilon \sin(\pi\theta/180) + B \cos(\pi\theta/180) = \frac{\lambda}{D_m}, \tag{3}$$

The mean grain size  $D_m$  and lattice strain  $\epsilon$  for the TiGa–ZnO samples deposited at different rf powers  $P_{rf}$  were calculated, and the results are plotted in Fig. 2b, c, respectively. Note from Fig. 2b that the  $D_m$  values are found to be about 58.2, 78.9, 83.1 and 72.4 nm for the TiGa–ZnO samples deposited at the rf power of 140, 165, 190 and 215 W respectively. The  $D_m$  increases first and subsequently decreases with the increment of rf power. The increase in grain size is attributed to the improvement of the TiGa–ZnO film crystallinity by the coalescence of small crystallites. From Fig. 2c, the tendency in the change

of the lattice strain  $\varepsilon$  is observed to be opposed to the mean grain size  $D_m$ . The  $\varepsilon$  values in the range of  $6.287 \times 10^{-4}$ – $8.999 \times 10^{-4}$  are observed with the variation of rf power from 140 to 215 W, and the lowest  $\varepsilon$  value of  $6.287 \times 10^{-4}$  is obtained at the rf power of 190 W. The decrease in  $\varepsilon$  can be attributed to the improvement of crystallinity and the increase of grain size. It is obvious that the TiGa–ZnO sample deposited at the rf power of 190 W possesses the best crystalline quality, with the narrowest  $B$  of  $0.1002^\circ$ , the largest  $D_m$  of 83.1 nm and the minimum  $\varepsilon$  of  $6.287 \times 10^{-4}$ . The results suggest that the crystal quality of the TiGa–ZnO thin films is strongly dependent upon the rf power.

Figure 3 shows the electrical resistivity ( $\rho$ ), carrier concentration ( $n_e$ ) and Hall mobility ( $\mu$ ) of the TiGa–ZnO samples deposited on glass substrates at different rf powers  $P_{rf}$ . As the rf power increases from 140 to 190 W, both carrier concentration and Hall mobility increase, which leads to the decrease of electrical resistivity of the deposited thin films. When the rf power is 190 W, the deposited thin film exhibits the lowest electrical resistivity of  $9.68 \times 10^{-4} \Omega \text{ cm}$ , along with the maximum carrier concentration and the highest Hall mobility of  $3.39 \times 10^{20} \text{ cm}^{-3}$  and  $18.98 \text{ cm}^2 \text{ V}^{-1} \text{ s}^{-1}$ , respectively. With further increasing the rf power over 190 W, however, the carrier concentration and Hall mobility begin to decrease, thus the electrical resistivity increases accordingly. This behaviour can be explained as follows. The sputtered species has low surface mobility on the substrate at low rf power, which results in degraded crystallinity and few Ti, Ga substitution, thus the deposited thin film has low

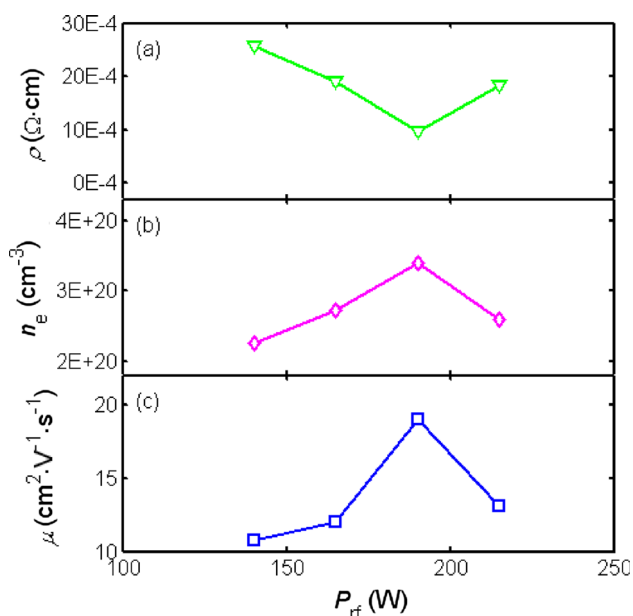


**Fig. 3** The values of  $\rho$ ,  $n_e$  and  $\mu$  for the thin films deposited at different rf powers

Hall mobility and carrier concentration. With the increasing rf power, the species kinetic energy increases, which improves the thin film crystallinity and Ti, Ga substitution. At the rf power of 190 W, the Hall mobility and carrier concentration reaches the maximum value. As the rf power further increases, due to the large mobile energies of the sputtered species, some species will be rebounded when colliding with the substrate, leading to the degradation of the film crystallinity, so carrier concentration and Hall mobility decrease, finally resulting in the decrease of electrical resistivity of the TiGa–ZnO thin films.

Figure 4 displays the transmittance ( $T$ ) spectra at normal incidence for the TiGa–ZnO samples deposited on glass substrates (TiGa–ZnO/substrate) at different rf powers  $P_{rf}$ . All the transmission spectra show interference pattern with sharp fall of transmittance at the band edge, which is an indication of good crystallinity. Because the reference used during optical measurements was air, the transmittance spectrum of uncoated glass substrate was also measured for a comparison (see Fig. 4). The average transmittance ( $T_{av}$ ) of the deposited thin films in the visible range has been calculated from the spectrum of the TiGa–ZnO-coated samples by subtracting that of the corresponding substrate, and the results are plotted in the inset in Fig. 4 as a function of rf power  $P_{rf}$ . The  $T_{av}$  increases with the increment of rf power from 140 to 190 W, and then significantly decreases when the rf power is over 190 W. The maximal  $T_{av}$  of 84.62 % is obtained at the rf power of 190 W. This enhancement in the optical transmittance is closely related to the improvement of crystallinity and the increase of

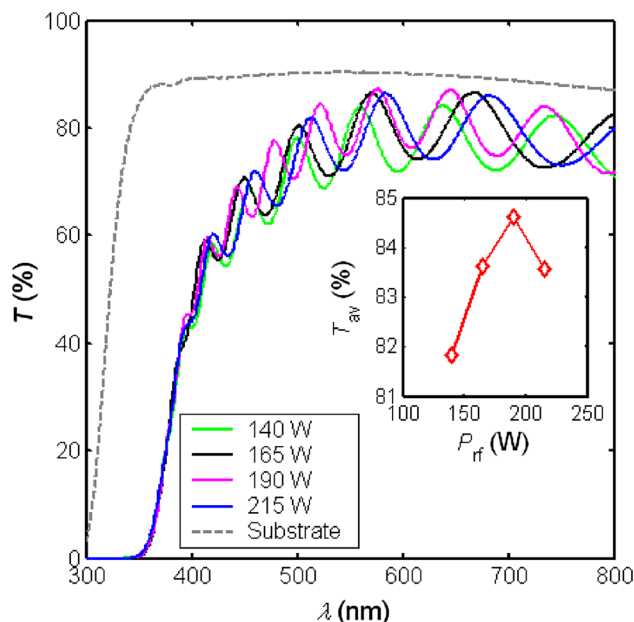


**Fig. 4** Optical transmission spectra of the thin films deposited on glass substrates at different rf powers

grain size for the deposited thin films. Near the absorption edge or in the strong absorption zone of the transmission spectra, the absorption coefficient ( $\alpha$ ) is related to the optical bandgap ( $E_g$ ) following the power-law behaviour of Tauc [45, 46]:

$$(\alpha h\nu)^2 = B_0(h\nu - E_g), \tag{4}$$

where  $h$  is the Planck constant,  $\nu$  is the frequency of the incident photon, and  $B_0$  is an energy-independent constant. The optical bandgap of the thin films can be calculated from the intercept of  $(\alpha h\nu)^2$  versus  $h\nu$  (the Tauc plot) for direct transitions [47, 48]. Figure 5 displays the Tauc plots of  $(\alpha h\nu)^2$  versus  $h\nu$  for all the samples. Better linearity for the Tauc plot was observed and the optical bandgap was determined by extrapolating the linear absorption edge part of the curve using Eq. (4). The dependence of optical bandgap on rf power is shown in the inset in Fig. 5. The  $E_g$  increases with rf power up to 190 W from about 3.374 to 3.503 eV. Then it decreases to 3.495 eV at rf power of 215 W. Clearly, these results are larger than that of undoped ZnO (about 3.270 eV). The widening of optical bandgap may be attributed to Moss–Burstein shift effect [49, 50]. This effect is due to that the conduction band filling in highly degenerate semiconductor makes the Fermi level exceed the conduction band minimum. Similar results for the doped ZnO thin films have been reported in the literature [51–54].

In order to evaluate the quality of the deposited TCO thin films, the figure of merit ( $F_{TC}$ ) is given by the following formula [55, 56]:

$$F_{TC} = \frac{1}{\rho \ln(1/T_{av})}, \tag{5}$$

where  $\rho$  is the electrical resistivity, and  $T_{av}$  is the average transmittance in the visible range. Figure 6 shows the variation of the figure of merit  $F_{TC}$  versus the rf power  $P_{rf}$  for the deposited TiGa–ZnO samples. As the rf power increases, the  $F_{TC}$  first increases and then decreases and reaches its maximum value of  $6.173 \times 10^3 \Omega^{-1} \text{ cm}^{-1}$  at the rf power of 190 W. The increase in figure of merit with rf power was due to decrease in the electrical resistivity and increase in optical transmittance. It is known that the higher the  $F_{TC}$ , the better quality of the TCO thin film. Thus, in this study, it can be concluded that the optimum rf power is 190 W, where the figure of merit is the highest.

From the measured transmittance spectra, the refractive index ( $n$ ) and extinction coefficient ( $k$ ) of the deposited thin films were determined using the pointwise unconstrained optimization method [36, 37]. Figure 7 shows the fitting curves of transmittance ( $T_{fit}$ ) for the TiGa–ZnO samples deposited on glass substrates at different rf powers  $P_{rf}$ . It is obvious from Fig. 7 that the fitting results are in satisfactory agreement with the measured data ( $T_{exp}$ ). Figure 8a, b display the  $n$  and  $k$  values of all the deposited thin films at different rf powers  $P_{rf}$ , respectively. The  $n$  decreases with the increase of wavelength ( $\lambda$ ), indicating that the deposited thin films possess the normal dispersion characteristics in the visible region. Meanwhile, the  $n$  is closely related to the rf power. For the TiGa–ZnO samples prepared at the rf power of 140, 165, 190 and 215 W, the  $n$  values are 2.144, 2.197, 2.138 and 2.166, respectively, when the wavelength  $\lambda = 545 \text{ nm}$ . From Fig. 8b, the  $k$  is observed to be very

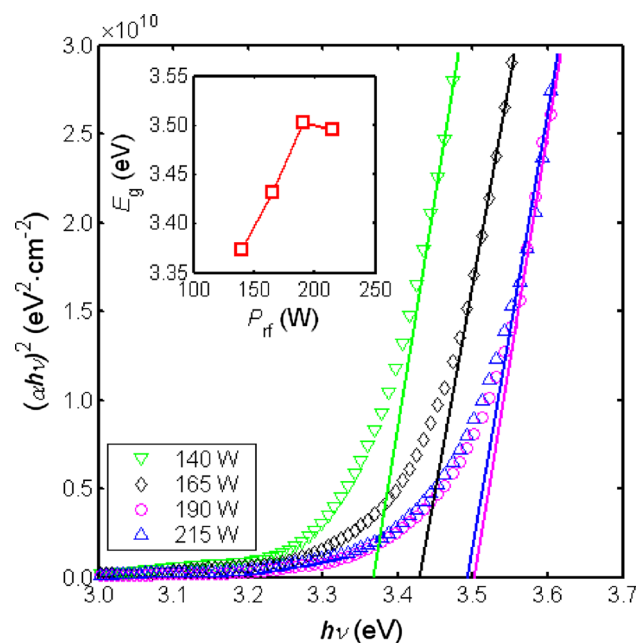


**Fig. 5** The  $(\alpha h\nu)^2 - h\nu$  plots for the thin films deposited at different rf powers

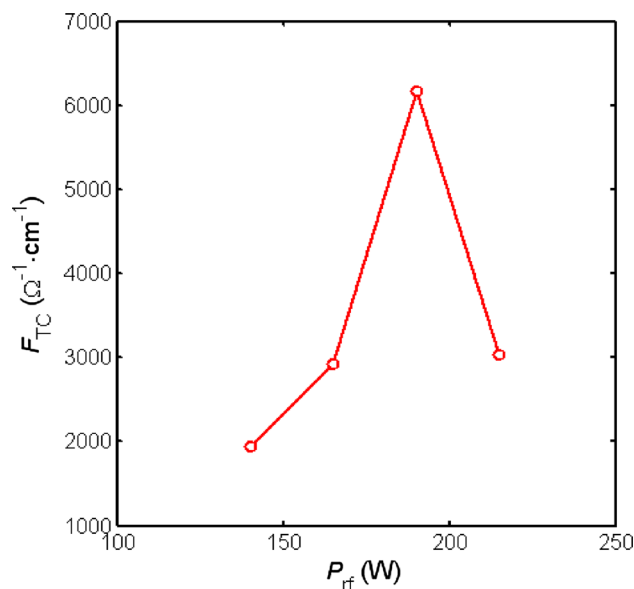


**Fig. 6** Figure of merit for the thin films deposited at different rf powers

small in the visible region, which indicates that the TiGa–ZnO thin films are almost transparent in the visible region. At the wavelength  $\lambda = 535$  nm, for the TiGa–ZnO samples

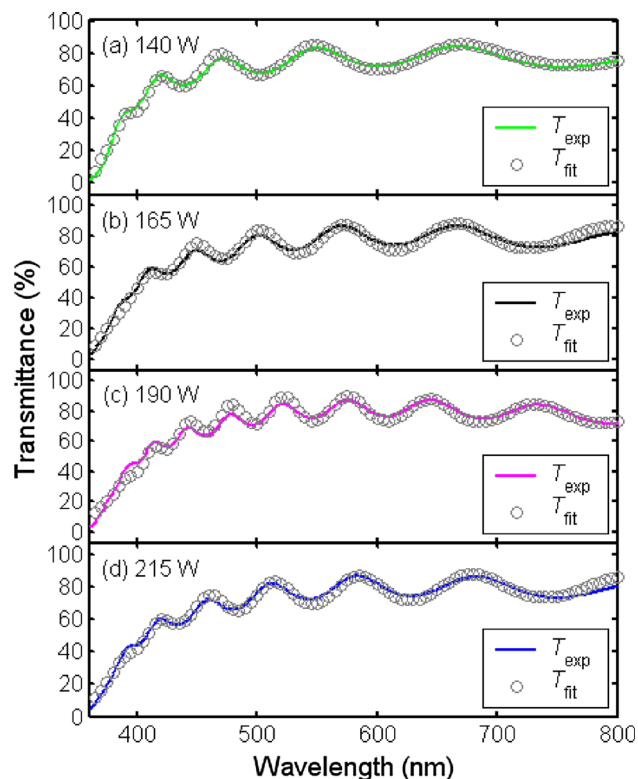


**Fig. 7** Fitting curves of transmittance for the thin films deposited on glass substrates at different rf powers

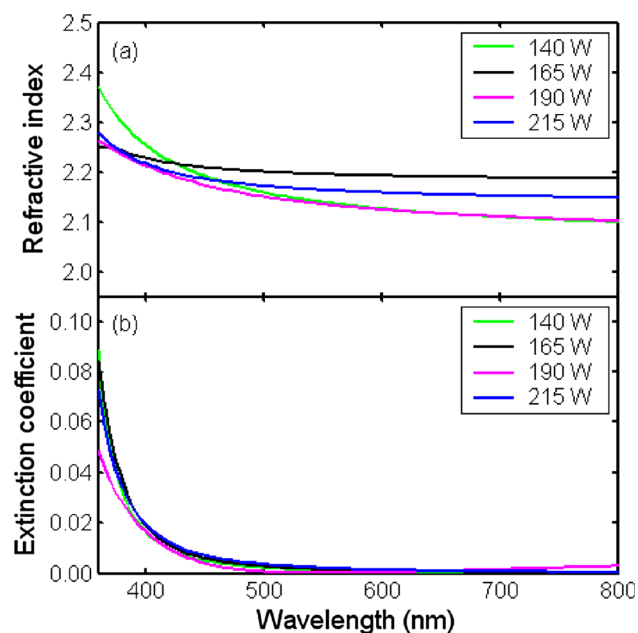


**Fig. 8** The values of  $n$  and  $k$  for the thin films deposited at different rf powers

deposited at the rf power of 140, 165, 190 and 215 W, the  $k$  values are  $1.271 \times 10^{-3}$ ,  $1.810 \times 10^{-3}$ ,  $6.927 \times 10^{-5}$  and  $2.586 \times 10^{-3}$ , and the corresponding values of absorption coefficient  $\alpha$  determined by the formula  $\alpha = 4\pi k/\lambda$  [57, 58] are  $2.985 \times 10^4$ ,  $4.251 \times 10^4$ ,  $1.627 \times 10^3$  and  $6.074 \times 10^4 \text{ m}^{-1}$ , respectively. The results in our work are consistent with that of the previous researches. Al-Hardan et al. [59] reported that the  $n$  values of undoped ZnO thin films were 1.94–2.20 obtained by the envelope method, and the  $n$  was about 1.97–2.08 measured by spectroscopic ellipsometry obtained by Hwang et al. [60] for gallium-doped ZnO thin films.

The refractive index dispersion of the deposited thin films was evaluated according to the Wemple–DiDomenico (W–D) single-oscillator model. It is well known from the dispersion theory that the refractive index  $n(\lambda)$  of the thin films in the region of low absorption can be expressed by the following relationship [61, 62]:

$$\frac{1}{n(\lambda)^2 - 1} = -\frac{1}{S_0 \lambda^2} + \frac{1}{S_0 \lambda_0^2}, \tag{6}$$

where  $S_0$  is the average oscillator strength, and  $\lambda_0$  is the average oscillator position. Figure 9 shows the curves of  $1/(n^2 - 1) - 1/\lambda^2$  for the TiGa–ZnO samples deposited on glass substrates at different rf powers  $P_{\text{rf}}$ . The data can be fitted into the straight lines, which indicates that the W–D single-

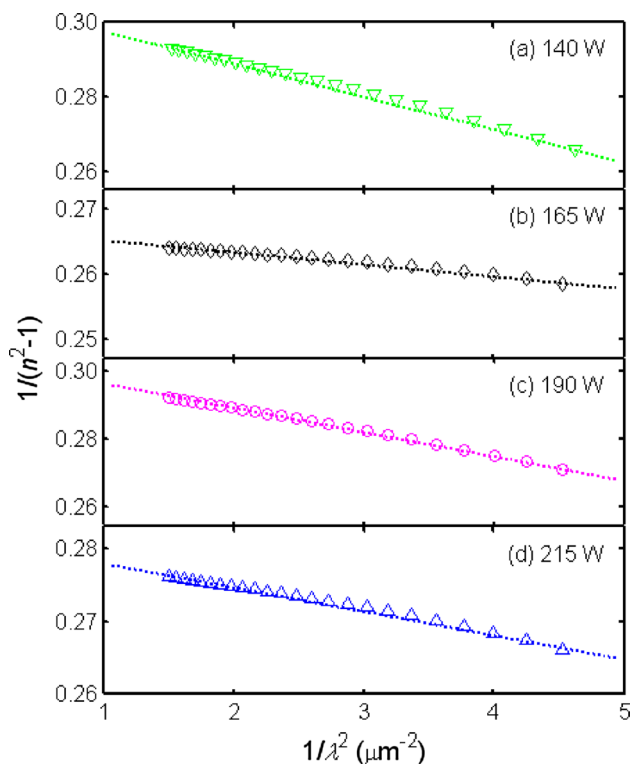


**Fig. 9** The  $1/(n^2 - 1) - 1/\lambda^2$  plots for the thin films deposited at different rf powers

oscillator model is applicable to the TiGa–ZnO thin films in the present work.

The frequency dispersion of complex dielectric constant ( $\epsilon$ ) characterizes completely the propagation, reflection and loss of light in multilayer structures. It provides us with information about the electronic structure of the material. Therefore, the complex dielectric constant  $\epsilon$  is an important quantity for the design of highly efficient optoelectronic devices. The real part of complex dielectric constant is associated with the term that describes how much the material will slow down the speed of light, and the imaginary part explains how a dielectric absorbs energy from an electric field due to the dipole motion. The real ( $\epsilon_r$ ) and imaginary ( $\epsilon_i$ ) parts of the complex dielectric constant ( $\epsilon = \epsilon_r - i\epsilon_i$ ) are related to the  $n$  and  $k$  values. The values of  $\epsilon_r$  and  $\epsilon_i$  can be determined by the following formulae [63]:

$$\epsilon_r = n(\lambda)^2 - k(\lambda)^2, \quad \epsilon_i = 2n(\lambda)k(\lambda), \quad (7)$$

Figure 10 shows the  $\epsilon_r$  and  $\epsilon_i$  values dependence of wavelength  $\lambda$  for the TiGa–ZnO samples deposited on glass substrates at different rf powers  $P_{rf}$ . It is clear that the variation of  $\epsilon_r$  follows the same trend as  $n$ , whereas the variation of  $\epsilon_i$  mainly follows the behavior of  $k$ . Both  $\epsilon_r$  and  $\epsilon_i$  gradually decrease with increasing wavelength  $\lambda$ , and for a given wavelength  $\lambda$ , the  $\epsilon_r$  values are higher than the  $\epsilon_i$  for all the deposited thin films. For the TiGa–ZnO samples deposited at the rf power of 140, 165, 190 and 215 W, the  $\epsilon$  are 4.587-i0.00474, 4.824-i0.00681, 4.567-i0.000258 and

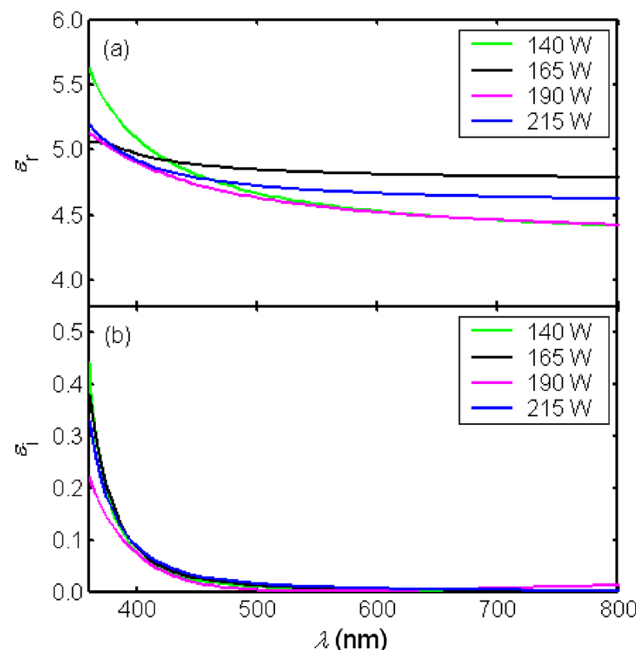


**Fig. 10** The values of  $\epsilon_r$  and  $\epsilon_i$  for the thin films deposited at different rf powers

4.687-i0.00939 respectively, when the wavelength  $\lambda = 550$  nm.

In physics, the dissipation factor ( $\tan\delta$ ) is a measure of loss-rate of power of a mechanical mode, such as an oscillation, in a dissipative system. For example, electric power is lost in all dielectric materials, usually in the form of heat. The dissipation factor  $\tan\delta$  can be calculated according to the following formula [63]:

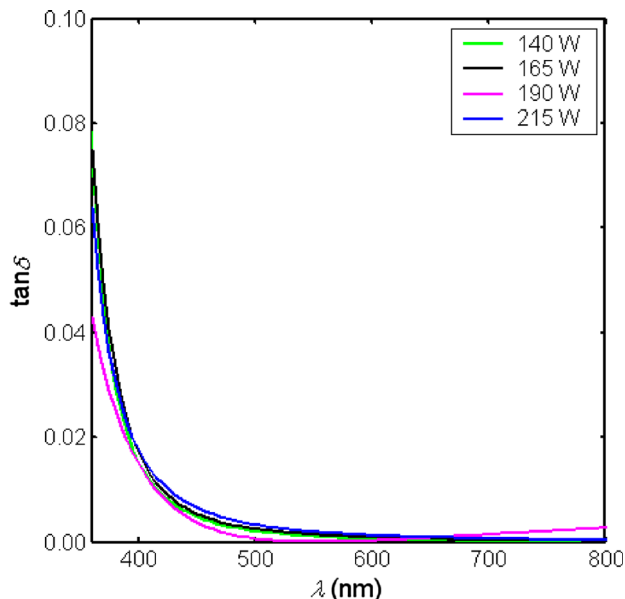
$$\tan\delta = \frac{\epsilon_i}{\epsilon_r}, \quad (8)$$

Figure 11 gives the dependence of  $\tan\delta$  on wavelength  $\lambda$  for the TiGa–ZnO samples deposited on glass substrates at different rf powers  $P_{rf}$ . As can be seen, the variation of  $\tan\delta$  follows the same trend as  $k$  and the  $\tan\delta$  value decreases monotonically with the increment of wavelength  $\lambda$ . The  $\tan\delta$  values are observed to be  $5.327 \times 10^{-3}$ ,  $6.060 \times 10^{-3}$ ,  $4.437 \times 10^{-3}$  and  $7.212 \times 10^{-3}$  for the TiGa–ZnO thin films deposited at the rf power of 140, 165, 190 and 215 W, respectively at wavelength  $\lambda = 445$  nm.

The absorption coefficient  $\alpha$  can be used to calculate the optical conductivity ( $\sigma_{opt}$ ) as follows [63]:

$$\sigma_{opt} = \frac{nc}{4\pi} \alpha, \quad (9)$$

where  $c$  is the velocity of light, and  $n$  is the refractive index. Figure 12 shows the variation of optical conductivity  $\sigma_{opt}$  as a function of photon energy  $h\nu$  for the TiGa–ZnO samples deposited on glass substrates at different rf powers  $P_{rf}$ . It is found that the optical conductivity increases with increasing the photon energy. The increase of optical conductivity  $\sigma_{opt}$  at high photon energies is due



**Fig. 11** The  $\tan\delta$  values of the thin films deposited at different rf powers

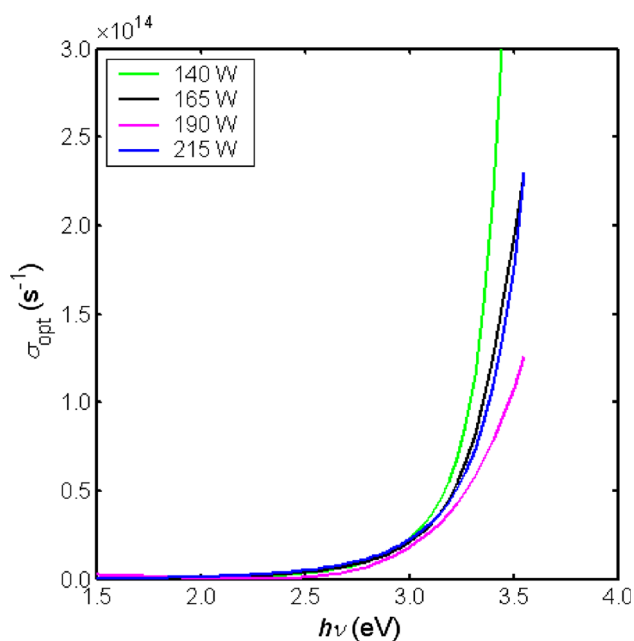


**Fig. 12** The  $\sigma_{\text{opt}}$  values of the thin films deposited at different rf powers

to the high absorbance of TiGa–ZnO thin films and also may be due to the electron excited by photon energy [64, 65]. When the photon energy  $h\nu$  is 3.10 eV ( $\lambda = 401.0$  nm), the  $\sigma_{\text{opt}}$  values are observed to be in the range of  $2.654 \times 10^{13}$ – $3.565 \times 10^{13}$  s $^{-1}$  with the variation of the rf power from 140 to 215 W, and the maximum  $\sigma_{\text{opt}}$  value of  $3.565 \times 10^{13}$  s $^{-1}$  is obtained at the rf power of 140 W. The result suggests that the rf power slightly affects the optical conductivity of the TiGa–ZnO thin films.

#### 4 Conclusions

In summary, transparent conducting TiGa–ZnO thin films were deposited by rf magnetron sputtering technique. The rf power dependence of the structural, electrical and optical properties for the deposited thin films was investigated by XRD, spectrophotometer, Hall effect measurement system and optical characterization methods. It is observed that the deposited thin films are polycrystalline and have preferred orientation along (002) direction. The crystal quality, structural and optoelectronic properties of the thin films are closely related to the rf power. As the rf power increases, the orientation factor of (002) plane, mean grain size, average visible transmittance, Hall mobility, carrier concentration and figure of merit are observed to increase initially and subsequently decrease, whereas the FWHM, lattice strain and electrical resistivity decrease firstly and then increase. The TiGa–ZnO thin film deposited at the rf power of 190 W exhibits the best crystal quality and

optoelectronic properties, with the largest mean grain size of 83.1 nm, the minimum lattice strain of  $6.287 \times 10^{-4}$ , the highest average visible transmittance of 84.62 %, the lowest electrical resistivity of  $9.68 \times 10^{-4}$   $\Omega$  cm and the maximum figure of merit of  $6.173 \times 10^3$   $\Omega^{-1}$  cm $^{-1}$ . The complex refractive index, complex dielectric constant, dissipation factor and optical conductivity of the deposited thin films were determined by optical characterization methods, and the dispersion behaviour of refractive index was studied by the W–D single-oscillator theory. It is found that the refractive index dispersion curves of thin films obey the W–D single-oscillator model. In addition, the optical bandgaps of the thin films were evaluated by means of the Tauc plots. The results show that the optical bandgaps are in the range of 3.374–3.503 eV, larger than that of undoped ZnO due to Burstein–Moss shift effect.

**Acknowledgments** This work was supported by the National Natural Science Foundation of China (No. 11504436), the Natural Science Foundation of Hubei (No. 2015CFB364) and the Fundamental Research Funds for the Central Universities (No. CZW14019), South-Central University for Nationalities.

#### References

1. Y.S. Song, N.J. Seong, K.J. Choi, S.O. Ryu, *Thin Solid Films* **546**, 271–274 (2013)
2. J. Owen, M.S. Son, K.H. Yoo, B.D. Ahn, S.Y. Lee, *Appl. Phys. Lett.* **90**, 033512 (2007)
3. X. Li, Y. Hu, *J. South-Cent. Univ. Natl. (Nat. Sci. Ed.)* **30**, 6–9 (2011)
4. H. Kim, J.S. Horwitz, W.H. Kim, A.J. Mäkinen, Z.H. Kafafi, D.B. Chrisey, *Thin Solid Films* **420–421**, 539–543 (2002)
5. H.T. Cao, C. Sun, Z.L. Pei, A.Y. Wang, L.S. Wen, R.J. Hong, X. Jiang, *J. Mater. Sci.: Mater. Electron.* **15**, 169–174 (2004)
6. S. Chen, S. Wei, *J. South-Cent. Univ. Natl. (Nat. Sci. Ed.)* **34**, 72–78 (2015)
7. J.J. Kim, J.H. Lee, J.Y. Bak, H.S. Kim, N.W. Jang, W.J. Lee, C.R. Cho, *J. Korean Phys. Soc.* **56**, 404–408 (2010)
8. J. Zhu, H. Chen, G. Saraf, Z. Duan, Y. Lu, S.T. Hsu, *J. Electron. Mater.* **37**, 1237–1240 (2008)
9. N. Yamamoto, H. Makino, S. Osone, A. Ujihara, T. Ito, H. Hokari, T. Maruyama, T. Yamamoto, *Thin Solid Films* **520**, 4131–4138 (2012)
10. J. Hu, Y. Zhou, H. Liu, L. Meng, M. Bao, Z. Song, *J. South-Cent. Univ. Natl. (Nat. Sci. Ed.)* **29**, 6–10 (2010)
11. C.Y. Tsay, K.S. Fan, C.M. Lei, *J. Alloys Compd.* **512**, 216–222 (2012)
12. M. Hjiri, L.E. Mir, S.G. Leonardi, A. Pistone, L. Mavilia, G. Neri, *Sens. Actuators B* **196**, 413–420 (2014)
13. A. Barhoumi, G. Leroy, B. Duponchel, J. Gest, L. Yang, N. Waldhoff, S. Guermazi, *Superlattices Microstruct.* **82**, 483–498 (2015)
14. T. Shibata, K. Unno, E. Makino, Y. Ito, S. Shimada, *Sens. Actuators A* **102**, 106–113 (2002)
15. D.A.A. Santos, H. Zeng, M.A. Macêdo, *Mater. Res. Bull.* **66**, 147–150 (2015)
16. S. Suzuki, T. Miyata, M. Ishii, T. Minami, *Thin Solid Films* **434**, 14–19 (2003)



17. S.D. Kirby, R.B. Van Dover, *Thin Solid Films* **517**, 1958–1960 (2009)
18. A. Suresh, P. Wellenius, A. Dhawan, J. Muth, *Appl. Phys. Lett.* **90**, 123512 (2007)
19. A. Davoodi, M. Tajally, O. Mirzaee, A. Eshaghi, *J. Alloys Compd.* **657**, 296–301 (2016)
20. D. Fang, K. Lin, T. Xue, C. Cui, X. Chen, P. Yao, H. Li, *J. Alloys Compd.* **589**, 346–352 (2014)
21. L. Zhang, J. Huang, J. Yang, K. Tang, B. Ren, Y. Hu, L. Wang, *Mater. Sci. Semicond. Process.* **42**, 277–282 (2016)
22. S. Aksoy, Y. Caglar, S. Ilcan, M. Caglar, *J. Alloys Compd.* **512**, 171–178 (2012)
23. R. Ebrahimi-fard, M.R. Golobostanfard, H. Abdizadeh, *Appl. Surf. Sci.* **290**, 252–259 (2014)
24. J. Liu, X. Chen, J. Fang, Y. Zhao, X. Zhang, *Sol. Energy Mater. Sol. Cells* **138**, 41–50 (2015)
25. X. He, L. Xiong, *J. South-Cent. Univ. Natl. (Nat. Sci. Ed.)* **30**, 70–73 (2011)
26. S.K. Kim, S.H. Kim, S.Y. Kim, J.H. Jeon, T.K. Gong, D.H. Choi, D.I. Son, D. Kim, *Ceram. Int.* **40**, 6673–6676 (2014)
27. H. Chen, J. Ding, W. Guo, *Ceram. Int.* **40**, 4847–4851 (2014)
28. S.B. Chen, *J. South-Cent. Univ. Natl. (Nat. Sci. Ed.)* **33**, 57–62 (2014)
29. X. Bie, J.G. Lu, L. Gong, L. Lin, B.H. Zhao, Z.Z. Ye, *Appl. Surf. Sci.* **256**, 289–293 (2009)
30. Q.-B. Ma, Z.-Z. Ye, H.-P. He, L.-P. Zhu, B.-H. Zhao, *Mater. Sci. Semicond. Process.* **10**, 167–172 (2007)
31. R.J. Ramalingam, G.S. Chung, *Mater. Lett.* **68**, 247–250 (2012)
32. H. Kato, M. Sano, K. Miyamoto, T. Yao, *J. Cryst. Growth* **237–239**, 538–543 (2002)
33. T. Yamada, T. Nebiki, S. Kishimoto, H. Makino, K. Awai, T. Narusawa, T. Yamamoto, *Superlattices Microstruct.* **42**, 68–73 (2007)
34. S.J. Henley, M.N.R. Ashfold, D. Cherns, *Surf. Coat. Technol.* **177–178**, 271–276 (2004)
35. F.L. Sun, S.W. Hui, *J. South-Cent. Univ. Natl. (Nat. Sci. Ed.)* **28**, 10–13 (2009)
36. E.G. Birgin, I. Chambouleyron, J.M. Martínez, *J. Comput. Phys.* **151**, 862–880 (1999)
37. Z. Zhong, Z. Teng, W. Hao, *J. South-Cent. Univ. Natl. (Nat. Sci. Ed.)* **32**, 58–64 (2013)
38. E. Fortunato, P. Barquinha, A. Pimentel, A. Goncalves, A. Marques, L. Pereira, R. Martins, *Thin Solid Films* **487**, 205 (2005)
39. J. Chen, D. Chen, J. He, S. Zhang, Z. Chen, *Appl. Surf. Sci.* **255**, 9413–9419 (2009)
40. J. Gu, L. Long, C. Lan, Z. Zhang, *J. South-Cent. Univ. Natl. (Nat. Sci. Ed.)* **33**, 78–84 (2014)
41. B.J. Jin, S.H. Bae, S.Y. Lee, S. Im, *Mater. Sci. Eng. B* **71**, 301–305 (2000)
42. J. Li, M. Gong, F. Zhao, Y. Xiang, L. Wei, Y. Zhang, *J. South-Cent. Univ. Natl. (Nat. Sci. Ed.)* **35**, 7–11 (2016)
43. J. Gu, L. Zhu, L. Lu, K. Hui, Z. Zhang, *J. South-Cent. Univ. Natl. (Nat. Sci. Ed.)* **35**, 91–96 (2016)
44. V. Arivazhagan, M.M. Parvathi, S. Rajesh, *Vacuum* **86**, 1092–1096 (2012)
45. Z. Huang, X. Liu, L. Wu, Y. Yuan, *J. South-Cent. Univ. Natl. (Nat. Sci. Ed.)* **35**, 17–22 (2016)
46. C.Y. Tsay, K.S. Fan, C.M. Lei, *J. Alloys Compd.* **512**, 216–222 (2012)
47. P.P. Sahay, S. Tewari, R.K. Nath, *Cryst. Res. Technol.* **42**, 723–729 (2007)
48. J. Hu, J. Yu, H. Li, M. Zhang, *J. South-Cent. Univ. Natl. (Nat. Sci. Ed.)* **31**, 11–14 (2012)
49. A.Z. Ben, M.L. El, K. Djessas, S. Alaya, *Mater. Sci. Eng. C* **28**, 613–617 (2008)
50. X.-Y. Li, H.-J. Li, Z.-J. Wang, H. Xia, Z.-Y. Xiong, J.-X. Wang, B.-C. Yang, *Opt. Commun.* **282**, 247–252 (2009)
51. C.Y. Tsay, C.W. Wu, C.M. Lei, F.S. Chen, C.K. Lin, *Thin Solid Films* **519**, 1516–1520 (2010)
52. S.B. Chen, C. Lan, *J. South-Cent. Univ. Natl. (Nat. Sci. Ed.)* **35**, 97–102 (2016)
53. S.R. Aghdaee, V. Soleimani, B. Tayebi, *Superlattices Microstruct.* **51**, 149–162 (2012)
54. Q.-B. Ma, Z.-Z. Ye, H.-P. He, S.-H. Hu, J.-R. Wang, L.-P. Zhu, Y.-Z. Zhang, B.-H. Zhao, *J. Cryst. Growth* **304**, 64–68 (2007)
55. J. Gu, L. Lu, L. Zhu, Z. Teng, Z. Zhang, *J. South-Cent. Univ. Natl. (Nat. Sci. Ed.)* **34**, 61–68 (2015)
56. A.K. Singh, *Optik* **124**, 2187–2190 (2013)
57. S. Cho, *Microelectron. Eng.* **89**, 84–88 (2012)
58. J. Gu, Z. Zhang, X. He, F. Sun, *J. South-Cent. Univ. Natl. (Nat. Sci. Ed.)* **28**, 30–33 (2009)
59. N.H. Al-Hardan, M.J. Abdullah, A.A. Aziz, H. Ahmad, M. Rashid, *Phys. B* **405**, 1081–1085 (2010)
60. Y. Hwang, S. Park, M. Kang, Y. Um, *Curr. Appl. Phys.* **14**, S23–S28 (2014)
61. S.H. Wemple, M. Didomenico Jr., *Phys. Rev. B* **3**, 1338–1351 (1971)
62. Z. Zhong, C. Lan, H. Wang, *J. South-Cent. Univ. Natl. (Nat. Sci. Ed.)* **33**, 51–54 (2014)
63. J.I. Pankove, *Optical Processes in Semiconductors* (Dover Publications, New York, 1975)
64. F. Yakuphanoglu, A. Cukurovali, I. Yilmaz, *Opt. Mater.* **27**, 1363–1368 (2005)
65. V. Dhanasekaran, T. Mahalingam, *J. Alloys Compd.* **539**, 50–56 (2012)